J. Fluid Mech. (2010), *vol.* 650, *pp.* 343–362. © Cambridge University Press 2010
doi:10.1017/S0022112009993697

Flow-induced vibrations of a deformable ring

KOUROSH SHOELE AND QIANG ZHU†

Department of Structural Engineering, University of California San Diego, La Jolla, CA 92093, USA

(Received 5 May 2009; revised 24 November 2009; accepted 25 November 2009; first published online 16 March 2010)

To understand flow-induced vibrations of deformable objects, we numerically investigate dynamics of a pressurized elastic ring pinned at one point within a uniform flow by using an immersed-boundary algorithm. The boundary of the ring consists of a fibre with no bending stiffness, which can be modelled as a linear spring with spring constant k and zero unstretched length. The vibration of the ring is decomposed into two parts: a pitching motion that includes a rigid-body rotation and a flexible bending motion in the transverse direction, and a tapping motion in the longitudinal direction. The pitching motion is dominated by the frequency of vortex shedding, whereas the primary frequency of the tapping motion is twice the frequency of vortex shedding. At the Reynolds number of 100, resonance is observed when $k \sim 0.2$ (k is normalized by the diameter of the undeformed ring, the speed of the upcoming flow and the fluid density). Across the resonance region, abrupt jumps in terms of the motion amplitudes as well as the hydrodynamic loads are recorded. Within the resonance region, the lift force demonstrates a beating phenomenon reminiscent of findings through reduced models and low-degree-of-freedom systems.

1. Introduction

Interactions between fluid and flexible structures are ubiquitous in nature (see e.g. Vogel 1996). In living creatures, structural flexibility provides an important mechanism to enhance their structural stability, locomotion capacity and physiological performance in surrounding flow fields. For example, through its body deformations a fish can extract energy from incoming vortex streets to reduce energy expenditure in swimming; in an extreme case, self-propulsion of a dead fish inside a vorticity field without muscle activation has been observed (Liao *et al.* 2003; Eldredge & Pisani 2008). In addition, the anisotropic flexibility of fish fins imparted by the distribution of embedded rays was found to significantly increase the propulsion efficiency (Zhu & Shoele 2008). Structural flexibility is also critical in the physiological function of cells. The deformability of erythrocyte (red blood cells or RBC), as determined by its composite membrane including a lipid bilayer and a protein skeleton made of actin and spectrin, is essential for maintaining its structural integrity and stability during circulation when it squeezes through capillaries (Mohandas & Evans 1994).

It is convenient to obtain physical insights about the underlying fluid–structure interaction mechanisms by studying flow interactions with idealized structures such as fibres or beams. Via experimental measurements and theoretical studies of the flow around a glass fibre, Alben, Shelley & Zhang (2002) observed drag reduction

† Email address for correspondence: qizhu@ucsd.edu

https://doi.org/10.1017/S0022112009993697 Published online by Cambridge University Press

attributed to streamlining effect as a result of structural flexibility (see also Alben, Shelley & Zhang 2004). Specifically, with sufficient structural deformation, the scaling law of drag with respect to the incoming flow speed U transits from U^2 to $U^{3/4}$. Similar behaviour has been reported in low-to-moderate Reynolds numbers through numerical simulations with an immersed-boundary algorithm (Zhu 2008).

Another type of simple structure under investigation is an elastic loop. By experimentally examining deformations and near-body flow fields of such a loop embedded in a fast flowing soap film at a Reynolds number of 5000, two distinctive states, a stationary state and a oscillatory state, were observed (Jung *et al.* 2006). The stationary state corresponds to a conventional von Kármán vortex street in the wake (i.e. 2S mode); in the oscillatory state, the body undergoes vibrations and two pairs of vortices are shed within each period (i.e. 2P mode). This phenomenon is similar to experimental observations and numerical simulations of a two-degree-of-freedom rigid cylinder undergoing vortex-induced vibrations, which displays multivortex shedding (including vortex triplets and quintuplets) in Reynolds numbers around 10 000 (Williamson & Roshko 1988; Williamson & Govardhan 2004; Dahl *et al.* 2007).

The primary purpose of our study is to correlate the dynamics (especially the flow-induced vibrations) of a bluff object with its structural flexibility. As an idealized example, we investigate the dynamics of a prestressed elastic ring in an incoming flow. Towards this end we apply an immersed-boundary (IB) algorithm, which is capable of solving fluid interactions with highly deformable structures. Immersed-boundary methods were first developed by Peskin (1977) for studying dynamics of immersed elastic fibres. In such an approach, these fibres are modelled as distributions of forces directly incorporated into the Navier–Stokes equations. By doing so, this method reduces computational efforts associated with re-meshing of fluidic grids and avoids mesh distortions encountered in highly flexible immersed structures (Hughes, Liu & Zimmerman 1981; Tezduyar 1992, 2001). In this study, we apply a formally second-order IB formulation (Lai & Peskin 2000), together with a spectral approach with high computational efficiency to simulate responses of an immersed ring. Specifically, with this method we consider the scenario about the flow-induced vibrations of a ring pinned at one point.

The rest of the paper is organized as follows. In § 2, we detail the immersed-boundary formulations and the numerical method, including an efficient spectral algorithm to solve the equations. This method is tested by comparing its predictions of flow around a fixed rigid cylinder with data from existing numerical and experimental studies, and by comparing its simulations of the free vibration of a flexible ring with asymptotic results. In both cases, excellent comparisons are achieved. Using this method, in § 3 we simulate flow-induced vibrations of a flexible ring pinned at one point and identify deformation modes and resonant responses. Finally, in § 4 conclusions are drawn.

2. Mathematical formulations and numerical methods

2.1. *Immersed-boundary formulations*

In our immersed boundary formulation, the ring is idealized as a loop of massless fibre and the structural force is transmitted directly to the surrounding fluid. As shown in figure 1, the fluid motion is described in a space-fixed coordinate system $\boldsymbol{x} = (x, y)$, in which the position of the ring is given as $\boldsymbol{x}(s, t)$, where s is a Lagrangian marker along the ring and t is the time. Note that s is a dimensionless parameter whose value changes from 0 to 1 along the ring. Mathematically, the fibre is modelled as singular distribution of force and incorporated into the Navier–Stokes equations

https://doi.org/10.1017/S0022112009993697 Published online by Cambridge University Press

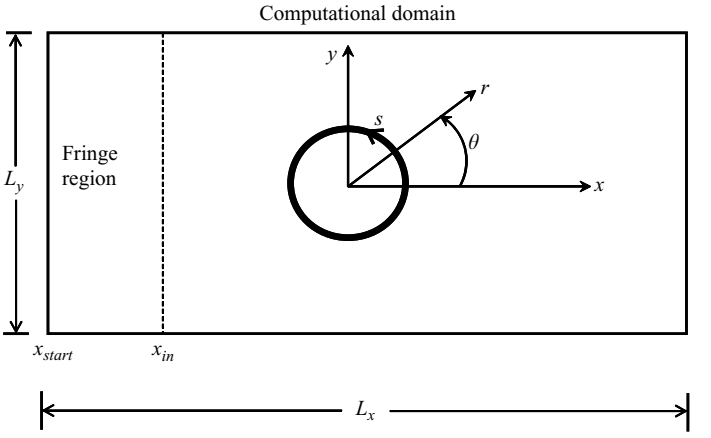


FIGURE 1. Definition of the computational domain.

as a forcing term $\boldsymbol{f}$, i.e.

$$\rho\left(\frac{\partial \boldsymbol{u}}{\partial t}+\boldsymbol{u}\cdot\nabla\mathbf{u}\right)=-\nabla p+\mu\nabla^2\boldsymbol{u}+\boldsymbol{f} \tag{2.1}$$

and

$$\nabla\cdot\boldsymbol{u}=0, \tag{2.2}$$

where ρ is the fluid density, μ is the dynamic viscosity, $\boldsymbol{u}=(u,v)$ is the flow velocity and p is the pressure. Let $\boldsymbol{X}(s,t)$ and $T(s,t)$ be the instantaneous location and the internal tension of the fibre respectively, we have

$$\boldsymbol{f}(\boldsymbol{x},t)=\oint_{\Gamma}\boldsymbol{F}(s,t)\delta[\boldsymbol{x}-\boldsymbol{X}(s,t)]\,\mathrm{d}s, \tag{2.3}$$

where Γ is the contour of the ring. δ is the Dirac function. And

$$\boldsymbol{F}(s,t)=\frac{\partial[T(s,t)\boldsymbol{\tau}(s,t)]}{\partial s},\quad \boldsymbol{\tau}=\frac{\partial\boldsymbol{x}/\partial s}{|\partial\boldsymbol{x}/\partial s|}. \tag{2.4}$$

Assuming that the fibre is linearly elastic with stiffness k and zero unstretched length, we have $T(s,t)\boldsymbol{\tau}(s,t)=k(\partial\boldsymbol{X}/\partial s)$. The overall hydrodynamic force on the ring is obtained by integrating the force $\boldsymbol{F}$ along the length of the ring.

Physically, the problem defined above resembles an idealized two-dimensional balloon with stretchable boundary. When the pressure difference between the inside and the outside regions of the balloon disappears, it has zero area and perimeter. The internal pressure required to swollen this balloon to a prescribed size increases with the elasticity k of its boundary.

2.2. *Numerical method*

To formulate the coupled problem of fluid motion and ring deformation, we apply two systems of grids: Eulerian grids (l,m) within the fluid domain (l is in the x direction and m is in the y direction) and Lagragian points j along s. To distinguish quantities described in these two systems, we denote those in the Eulerian system by two indexes (e.g. $\boldsymbol{x}_{lm}$) and those in the Lagrangian system by a single index (e.g. $\boldsymbol{F}_j$). The ring is discretized with a fixed grid size of Δs ($\Delta s=1/N_s$, where N_s is the number of elements along the ring), and the fluid domain is discretized with grid

https://doi.org/10.1017/S0022112009993697 Published online by Cambridge University Press

sizes $\Delta x = \Delta y = h$. Transformations of force and velocity between the fixed Eulerian grids ($\boldsymbol{f}_{lm}$ and $\boldsymbol{u}_{lm}$) and the Lagrangian points ($\boldsymbol{F}_j$ and $\boldsymbol{U}_j$) are achieved by using the regularized discrete delta function, e.g.

$$\boldsymbol{f}_{lm} = \sum_j \boldsymbol{F}_j \delta_h(\boldsymbol{x}_{lm} - \boldsymbol{X}_j)\Delta s, \tag{2.5}$$

$$\boldsymbol{U}_j = \sum_{l,m} \boldsymbol{u}_{lm} \delta_h(\boldsymbol{x}_{lm} - \boldsymbol{X}_j)\Delta x \Delta y. \tag{2.6}$$

The Dirac function is approximated by

$$\delta_h(\boldsymbol{x}) = \frac{1}{h^2}\phi\left(\frac{x}{h}\right)\phi\left(\frac{y}{h}\right), \tag{2.7}$$

where we apply the four-point approximation of the Dirac function with

$$\phi(r) = \begin{cases} \frac{1}{8}(3 - 2|r| + \sqrt{1 + 4|r| - 4r^2}), & 0 \leqslant |r| < 1, \\ \frac{1}{8}(5 - 2|r| + \sqrt{-7 + 12|r| - 4r^2}), & 1 \leqslant |r| < 2, \\ 0, & 2 \leqslant |r|. \end{cases} \tag{2.8}$$

The Navier–Stokes equations (2.1) and (2.2) are solved by using the formally second-order algorithm developed by Lai & Peskin (2000).

In long-term simulations, the conventional immersed-boundary algorithm suffers from spurious volume loss for problems with closed surfaces. In order to mitigate this effect, we adopt the method proposed by Peskin & Printz (1993) and replace the central difference operator $\boldsymbol{D}$ in the formulation described by Lai & Peskin (2000) with a modified operator $\mathscr{D}$. For example, at a grid (l, m) the divergence of $\boldsymbol{u}$ is calculated as

$$(\mathscr{D} \cdot \boldsymbol{u})_{lm} = \frac{1}{h^2}\int\int_{B_{lm}} \nabla \cdot \boldsymbol{u}(\mathbf{x}', t)\,\mathrm{d}\boldsymbol{x}', \tag{2.9}$$

where B_{lm} represents a box centred at the grid (l, m) with length h at each side. Thus defined, $\mathscr{D}$ is essentially a local gradient averaging operator. For numerical efficiency, (2.9) is evaluated by using

$$(\mathscr{D} \cdot \boldsymbol{u})_{lm} = \sum_{l'm'} \boldsymbol{u}_{l'm'} \cdot \boldsymbol{H}(\mathbf{x}_{l'm'} - \boldsymbol{x}_{lm})\, h^2, \tag{2.10}$$

where

$$\boldsymbol{H}(\boldsymbol{x}) = \frac{1}{h^2}\int\int_{B_{00}} \nabla\delta_h(\boldsymbol{x} + \boldsymbol{x}')\,\mathrm{d}\boldsymbol{x}'. \tag{2.11}$$

Here B_{00} is a box centred at $(0, 0)$ with length h at each side. We have

$$\boldsymbol{H}(\boldsymbol{x}_{l'm'} - \boldsymbol{x}_{lm}) = \frac{1}{h^3}\begin{bmatrix} \gamma_{l'-l}\kappa_{m'-m} \\ \gamma_{m'-m}\kappa_{l'-l} \end{bmatrix}, \tag{2.12}$$

https://doi.org/10.1017/S0022112009993697 Published online by Cambridge University Press

where $\gamma_l = \phi(l + (1/2)) - \phi(l - (1/2))$ and $\kappa_l = \int_{-1/2}^{1/2} \phi(l + r)\,\mathrm{d}r$. Using (2.8), γ and κ can be obtained explicitly as

$$\gamma_l = \begin{cases} \frac{2-\sqrt{2}}{8}, & l = -2, \\ \frac{\sqrt{2}}{4}, & l = -1, \\ 0, & l = 0 \quad \text{or} \quad |l| > 2, \\ -\frac{\sqrt{2}}{4}, & l = 1, \\ -\frac{2-\sqrt{2}}{8}, & l = 2, \end{cases} \tag{2.13}$$

and

$$\kappa_l = \begin{cases} \frac{4-\pi}{64}, & l = -2, \\ \frac{1}{4}, & l = -1, \\ \frac{12+\pi}{32}, & l = 0 \quad \text{or} \quad |l| > 2, \\ \frac{1}{4}, & l = 1, \\ \frac{4-\pi}{64}, & l = 2. \end{cases} \tag{2.14}$$

More details about the implementation of the IB method can be found in the literature (see e.g. Peskin 2002).

Doubly periodic conditions are implemented in both x and y directions. In order to prevent disturbances from neighbouring domains to enter the computational domain, we apply the fringe-region method introduced by Spalart (1988*a*,*b*). In this method, we install a fringe region in the entrance of the computational domain between x_{start} and x_{in} (see figure 1). The disturbances leaving the neighbouring domain are damped out when travelling form x_{start} to x_{in} and the flow velocity is gradually adjusted to the inflow velocity $\boldsymbol{u}_\infty$. To achieve this, within the fringe region the momentum equation (2.1) is modified by including an x-dependent forcing term. This forcing term is expressed as $\boldsymbol{f}_{frg}(x) = \lambda(x)(\boldsymbol{u}_\infty - \boldsymbol{u})$, where λ is a fringe function flat in most of the fringe region while decaying smoothly to zero at the boundaries of the fringe region. Here we choose the fringe function to be

$$\lambda(x) = \lambda_0 \left[S\left(\frac{x - x_{start}}{d_r}\right) - S\left(\frac{x_{in} - x}{d_f}\right) + 1 \right], \tag{2.15}$$

where

$$S(x) = \begin{cases} 0, & x \leqslant 0, \\ \dfrac{1}{1 + \mathrm{e}^{\frac{1}{1-x} + \frac{1}{x}}}, & 0 < x < 1, \\ 1, & x \geqslant 1. \end{cases} \tag{2.16}$$

Here d_r and d_f characterize the widths of increasing and decreasing regions of $\lambda(x)$, respectively. Note that λ_0 is the magnitude of the damping, which is determined through numerical tests. In our simulations, the fringe region occupies 1/8 of the computational domain. In addition, sensitivity tests have been performed to ensure that the computational domain is sufficiently large so that boundary effects are negligible.

The discretized Navier–Stokes equations are linear and therefore can be solved efficiently in Fourier space. For numerical efficiency, fast Fourier transformations (FFT) with periodic boundary condition are applied for solving the system of equations. More details on spectral solver are found in Peskin & Printz (1993).

https://doi.org/10.1017/S0022112009993697 Published online by Cambridge University Press

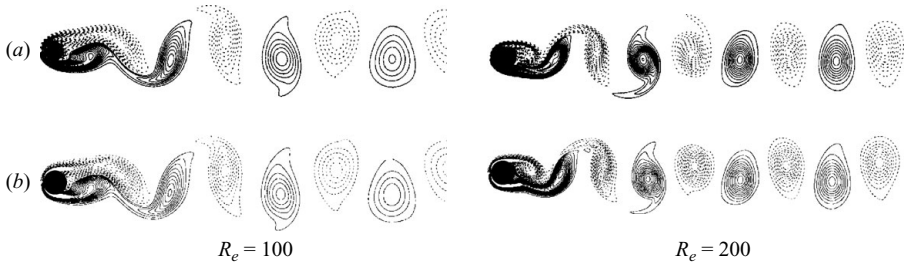


FIGURE 2. Comparison between the wakes (illustrated by contours of vorticity) behind a rigid cylinder predicted by (*a*) Saiki & Biringen (1996) using a virtual boundary method and (*b*) the current method. Negative vorticity is shown by dashed lines.

2.3. *Method testing*

To corroborate the validity and accuracy of the immersed-boundary algorithm developed above, below we use this method to study two cases, flow around a fixed rigid cylinder and free vibrations of a flexible ring, and compare our predictions with results from experiments, other numerical models and asymptotic studies.

2.3.1. *Flow around a rigid cylinder*

We first consider flow around a fixed and rigid cylinder. In our immersed-boundary approach, the rigid cylinder is represented by applying the boundary forcing term $\boldsymbol{F}(s,t)$ as

$$\boldsymbol{F}(s,t) = K\left[\boldsymbol{X}_{cyl}(s) - \boldsymbol{X}(s,t)\right], \tag{2.17}$$

where $\boldsymbol{X}_{cyl}(s)$ represents a circular cylinder with diameter $2R$. The constant K is chosen to be sufficiently large to prevent any significant displacement of $\boldsymbol{X}(s,t)$ from $\boldsymbol{X}_{cyl}(s)$. The incoming uniform flow velocity is $\boldsymbol{u}_\infty = (U,0)$, corresponding to a Reynolds number $R_e = 2\rho UR/\mu$. The numerical parameters used in these testing simulations are $N_1 \times N_2 = 564 \times 450$, the number of elements along the fibre $N_s = 56$, $L_x = 65R$ and $L_y = 52R$.

In figure 2, we plot the wake behind the rigid cylinder at $R_e = 100$ and $R_e = 200$ as obtained by the current method. Also plotted are predictions from Saiki & Biringen (1996) using a virtual boundary approach. It is seen that the two results are almost identical to each other.

For quantitative comparisons, we obtain the first harmonic lift coefficient $C_L^{(1)} = F_L^{(1)}/\rho U^2 R$, the mean drag coefficient $\overline{C}_D = \overline{F}_D/\rho U^2 R$ and the Strouhal number $St = 2f_s R/U$ (f_s is the vortex shedding frequency), and compare with data from other numerical models and experiments. The first harmonic lift force $F_L^{(1)}$ and the mean drag force $\overline{F}_D$ are evaluated as

$$F_L^{(1)} = 2f_s \mathrm{Re}\left\{\int_{t_0}^{t_0+1/f_s} F_y(t)\mathrm{e}^{2\mathrm{i}\pi f_s t}\,\mathrm{d}t\right\}, \tag{2.18}$$

$$\overline{F}_D = f_s \int_{t_0}^{t_0+1/f_s} F_x(t)\,\mathrm{d}t. \tag{2.19}$$

As shown in table 1, the predictions of S_t, $C_L^{(1)}$ and $\overline{C}_D$ of this model are in agreement with the listed benchmark results.

https://doi.org/10.1017/S0022112009993697 Published online by Cambridge University Press

		St	$\overline{C}_D$	$C_L^{(1)}$
$Re = 100$	Berger & Wille (1972)	0.16–0.17		
	Engelman & Jaminia (1990)	0.173	1.411	
	Gresho *et al.* (1984)	0.18	1.76	
	Karniadakis & Triantafyllou (1992)	0.168		
	Kim, Kim & Choi (2001)	0.165	1.33	
	Papaioannou *et al.* (2008)	0.170		
	Lai & Peskin (2000)	0.165	1.45	0.33
	Roshko (1954)*	0.164		
	Saiki & Biringen (1996)	0.171	1.26	
	Tseng & Ferziger (2003)	0.164	1.42	0.29
	Williamson (1988)*	0.164		
	Current method	0.166	1.46	0.33
$Re = 200$	Liu, Zheng & Sung (1998)	0.192	1.31	0.69
	Lai & Peskin (2000)	0.190		
	Linnick & Fasel (2005)	0.197	1.34	0.69
	Papaioannou *et al.* (2008)	0.200		
	Roshko (1954)*	0.190		
	Taira & Colonius (2007)	0.196	1.35	0.68
	Williamson (1988)*	0.196		
	Current method	0.198	1.39	0.70

* Experimental results.

TABLE 1. Comparison of the Strouhal number and the lift/drag coefficients of flow past a rigid cylinder predicted by the current numerical model with results from previous studies.

2.3.2. *Free vibrations of a flexible ring: comparisons with asymptotic results*

We consider the free vibration of a flexible ring in still fluid and obtain the frequencies and decaying rates of the oscillation modes. This problem can be alternatively solved by a perturbation approach (Cortez *et al.* 2004). Results obtained from this asymptotic method are compared with the IB predictions.

In its static position, the ring is circular so that in a cylindrical coordinate system (r, θ) its configuration is expressed as $r(\theta, t) = R$. Numerically, we choose $L_x = L_y = 5R$, $N_1 = N_2 = 256$ and $N_s = 720$. With these parameters, no significant disturbances from neighbouring domains are observed within the duration of simulation (even though no fringe region is applied in these simulations).

An initial deformation is applied so that at $t = 0$, the shape of the ring is distorted to $r(\theta, 0) = R(1 + \epsilon \cos q\theta)$, where q is an integer representing the wavenumber around the ring and $\epsilon \ll 1$. The ring is then released and its free vibrations as well as the surrounding flow field are recorded. It is observed that the ring undergoes a standing-wave deformation with the prescribed wavenumber q. Correspondingly, the near-body flow field contains $2q$ cells of circulation, with neighbouring cells rotating in opposite directions (figure 3). We note that in the case with $q = 2$, the flow field also resembles simulated results of the flow around a ring undergoing prescribed deformations by using a vortex particle method (Zhang & Eldredge 2009) (see their figure 2).

On the basis of the recorded time history of the ring deformation, we obtain the frequency β and the decaying rate α of mode q by assuming that the time dependency of the motion is in the form $e^{\gamma t}$, where $\gamma = \alpha + i\beta$. In order to extract β and α from the results, we record the position of a point on the ring with a fixed θ ($\theta = \theta_0$). Its radial motion is extracted as $r(\theta_0, t)$. This time-varying function is then fitted to the standard form of a linear oscillator $R(1 + \epsilon e^{\alpha t} \cos \beta t \cos q\theta)$ by using the least-square scheme.

https://doi.org/10.1017/S0022112009993697 Published online by Cambridge University Press

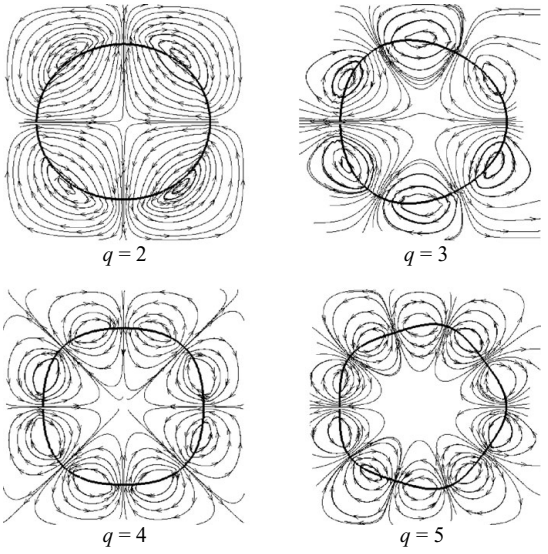


FIGURE 3. Snapshots of the ring deformation and the surrounding flow field (shown in streamlines) of modes $q = 2, 3, 4$ and 5. For IB simulations, the initial deformation of the ring is $r(\theta, t = 0) = R(1 + 0.05 \cos q\theta)$.

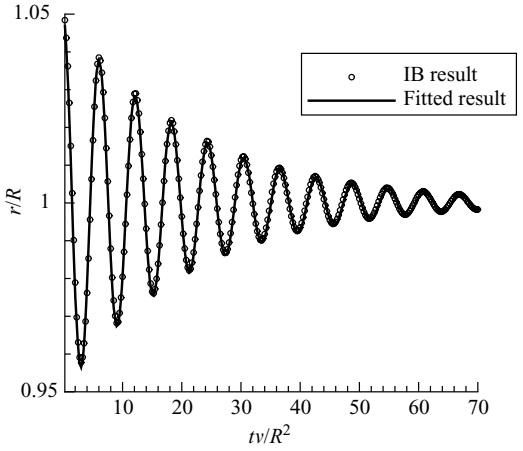


FIGURE 4. IB prediction of the radial motion of a point on the ring located at $\theta = \theta_0 = \pi$ with initial disturbance $r(\theta, t = 0) = R(1 + 0.05 \cos 4\theta)$, together with the least square fit to $R(1 + 0.05e^{\alpha t} \cos \beta t \cos 4\theta_0)$ with $\alpha R^2/\nu = -46.9$ and $\beta R^2/\nu = 1029$. Note that $kR/(\rho\nu^2) = 2.51 \times 10^5$.

As shown in figure 4, with this technique, perfect matching between the original curve and the least-square fit is obtained. Overall, eight different points evenly distributed along the ring are tested and the differences in the measured α and β values are found to be negligible.

As mentioned above, the free vibration of an elastic ring can be alternatively solved by an asymptotic method. Following Cortez *et al.* (2004), the problem can be solved by using a perturbation approach assuming that the deformation of the ring is small. At the first order with respect to ring deformation, the linearized problem is solved and from which the leading-order approximation of the frequency β and the decaying

https://doi.org/10.1017/S0022112009993697 Published online by Cambridge University Press

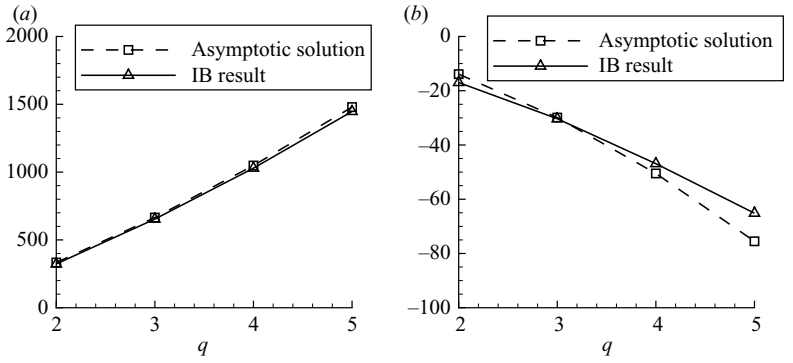


FIGURE 5. (*a*) The frequency β and (*b*) the decaying rate α of modes $q = 2, 3, 4$ and 5. Both α and β are normalized by ν/R^2. For IB simulations, the initial deformation of the ring is $r(\theta, t = 0) = R(1 + 0.05 \cos q\theta)$ and $kR/(\rho\nu^2) = 2.51 \times 10^5$.

rate α are evaluated. A detailed description of this asymptotic solution is provided in the Appendix. Figure 5 shows the comparison between the numerical prediction and the asymptotic approximation of α and β of four different modes, $q = 2, 3, 4$ and 5. The two predictions match well with each other.

3. Results

We consider a configuration with one point of the ring pinned in space within an incoming uniform flow $\boldsymbol{u}_\infty = (U, 0)$. To mitigate transient effects, in the beginning of the simulation the flow speed is increased slowly from zero to U. Hereafter, the problem is normalized by assuming that the diameter of the undeformed ring $2R$, the incoming flow speed U and the fluid density ρ are all 1. The Reynolds number based upon $2R$ is chosen to be 100. The numerical parameters are $L_x = 32$, $L_y = 8$, $N_x = 512$, $N_y = 128$ and $N_s = 80$.

3.1. *The mean deformation*

Our simulations demonstrate that in such a configuration the ring motion contains a mean deformation, and upon it, oscillatory deformations as well as a rigid-body rotation around the pinning point. The oscillatory deformations and the rotation are activated by the periodic shedding of vortices from the ring and the subsequent variations of the drag force, the lifting force and the pitching moment. In this configuration, a cusp is formed at the pinning point. Numerical tests have been performed to confirm that the fluid grids are sufficiently dense so that the flow field near the cusp remains smooth and regular. In particular, in highly flexible cases we also carefully monitored the positions of Lagrangian points near the cusp so that the distances between them are sufficiently large in comparison to the size of the fluid grids (otherwise the two points may 'stick' together because of the approximations in the immersed-boundary method).

Self-induced and self-limiting oscillations are observed. With most values of k, the base frequency of the ring motion remains the same as the vortex shedding frequency. Thus, the mean deformation is extracted via averaging over one vortex shedding period. The mean deformations of the ring with three different stiffnesses ($k = 1.0$, 0.3 and 0.1) obtained in this manner are displayed in figure 6. As we see, when the stiffness is reduced the mean configuration of the ring changes from a circle to a teardrop shape. Within a small range of k ($0.15 < k < 0.25$), however, no simple

https://doi.org/10.1017/S0022112009993697 Published online by Cambridge University Press

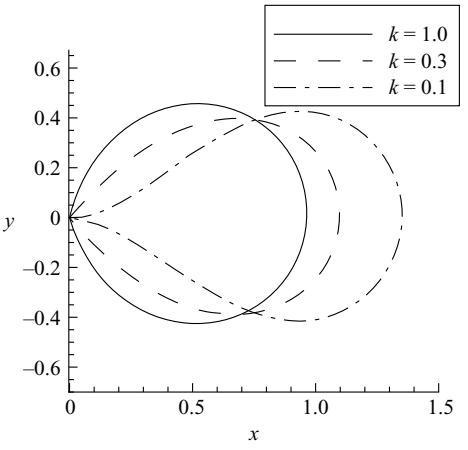


FIGURE 6. Mean deformations of ring with different k.

periodic ring motion is observed and subsequently the mean deformation can not be determined. This corresponds to the scenario of fluid–structure resonance to which detailed studies and discussions are dedicated (see § 3.4).

3.2. *The oscillatory deformations*

After subtracting the mean deformation, the oscillatory modes within the motion are decomposed via Fourier analysis. Let $\boldsymbol{X}(s_j, t) = (x(s_j, t), y(s_j, t))$ $(j = 1, \ldots, N_s)$, with Fourier expansion we express $x(s_j, t)$, $y(s_j, t)$ as a linear combination of M Fourier modes as

$$x(s_j, t) \doteq \sum_{m=1}^{M} A_m^x(s_j) \cos\left[\omega_m t + \phi_m^x(s_j)\right] \tag{3.1}$$

and

$$y(s_j, t) \doteq \sum_{m=1}^{M} A_m^y(s_j) \cos\left[\omega_m t + \phi_m^y(s_j)\right], \tag{3.2}$$

where $\omega_m = 2\pi m / M\Delta T$ (ΔT is the sampling interval). This Fourier analysis allows us to obtain responses at a certain harmonic by filtering out other components.

In figure 7, we plot frequencies of the dominant modes of the ring deformation. The first mode has the same frequency f_s as the vortex shedding frequency, and the second mode has frequency $2f_s$. Deformations at these two harmonics are obtained from (3.1) and (3.2) and displayed in figures 8 and 9 at two typical cases: $k = 0.1$ and $k = 0.4$. It is seen that at $k = 0.1$, the first harmonic motion corresponds mostly to deformations in the transverse direction (hereafter the bending motion), while the second harmonic motion is negligibly small. At $k = 0.4$, on the other hand, the first harmonic motion is dominated by a rigid-body pitching motion around the pinning point. In the second harmonic, a longitudinal deformation characterized by a stretch and compression of the ring appears (referred to as the *tapping motion*). The relation between the frequencies of longitudinal and transverse motions is consistent with the experiment by Jung *et al.* (2006) about the flow-induced oscillations of an elastic loop, in which a figure-of-eight motion pattern for the centre of the loop was observed.

As a metric of the magnitude of each mode, we define an 'energy norm' of its modal response as $E_m = \sqrt{(1/N_s)\sum_{j=1}^{N_s} [A_m^x(s_j)^2 + A_m^y(s_j)^2]}$. Thus defined, the energy norm

https://doi.org/10.1017/S0022112009993697 Published online by Cambridge University Press

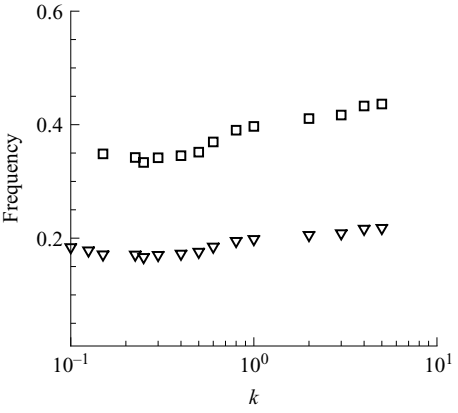


FIGURE 7. First two dominant frequencies of the ring motion and the hydrodynamic forces vs. k: (∇) first harmonic, corresponding to vortex shedding frequency and the dominant frequency of the lift force and the transverse motion; ($\square$) second harmonic, corresponding to the dominant frequency of the drag force and the longitudinal motion.

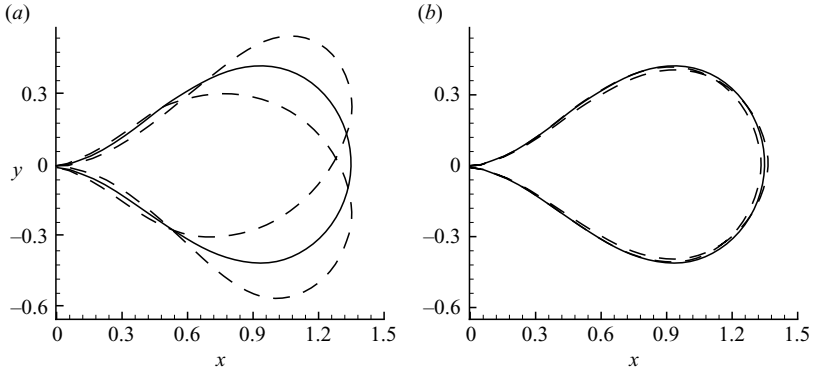


FIGURE 8. Snapshots of the maximum ring deformations superposed upon the mean configuration (shown by (——)) at (a) the first harmonic (f_s) and (b) the second harmonic ($2f_s$). $k = 0.1$.

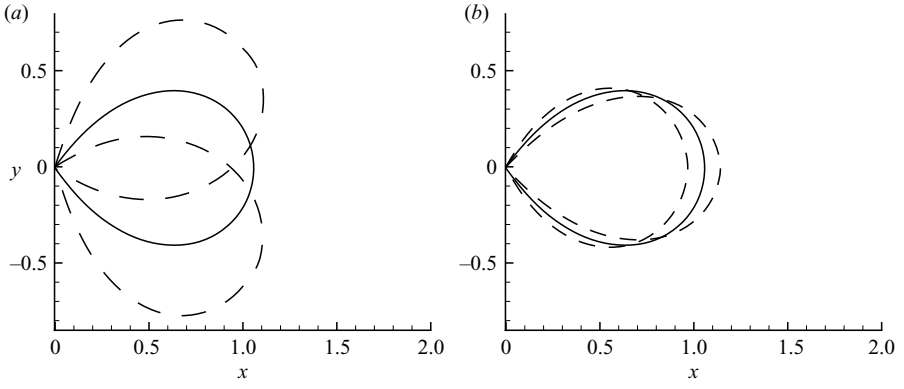


FIGURE 9. Snapshots of the maximum ring deformations superposed upon the mean configuration (shown by (——)) at (a) the first harmonic (f_s) and (b) the second harmonic ($2f_s$). $k = 0.4$.

https://doi.org/10.1017/S0022112009993697 Published online by Cambridge University Press

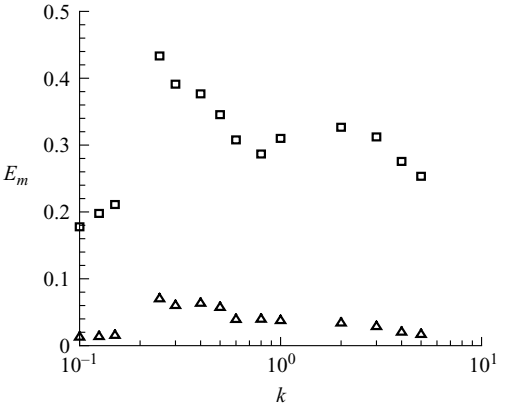


FIGURE 10. Energy norms of the first two dominant modes vs. k. □, first harmonic; △, second harmonic.

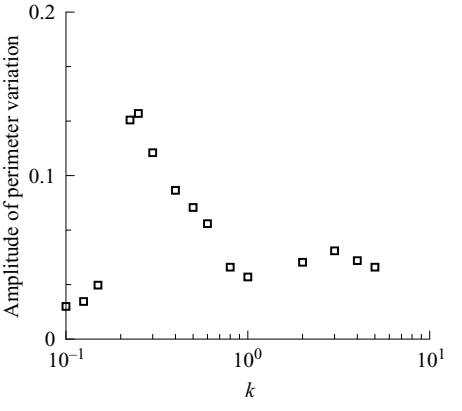


FIGURE 11. Amplitude of perimeter change in the second harmonic versus k.

of the ring motions in the first and the second harmonics is displayed in figure 10. As clearly shown, both of them reach their maximum values as k approaches 0.25 from above. Beneath that critical value of k, an abrupt drop in the motion is observed. When k is smaller than 0.15, the second harmonic motion becomes negligibly small, consistent with what is shown in figure 8.

Another important value that characterizes the ring deformation is its perimeter. Fourier analysis based upon the recorded time history of this value shows that its variation concentrates in the second harmonic. This suggests that the length change is mostly attributed to the tapping motion. In this frequency, the amplitude of the perimeter change at different values of k is plotted in figure 11. Near $k = 0.25$, a peak is also observed.

3.3. *The drag and lift forces*

Figure 12 displays the dominant harmonic components of the drag coefficient and the lift coefficient as functions of the structural stiffness k. For comparison, in the same figure we also show the corresponding values of the mean drag coefficient and the first harmonic lift coefficient of a fixed rigid cylinder with the same diameter as the undeformed ring. It has been shown that the mobility and structural flexibility of the ring greatly increase the mean drag. This is mostly attributed to the increase

https://doi.org/10.1017/S0022112009993697 Published online by Cambridge University Press

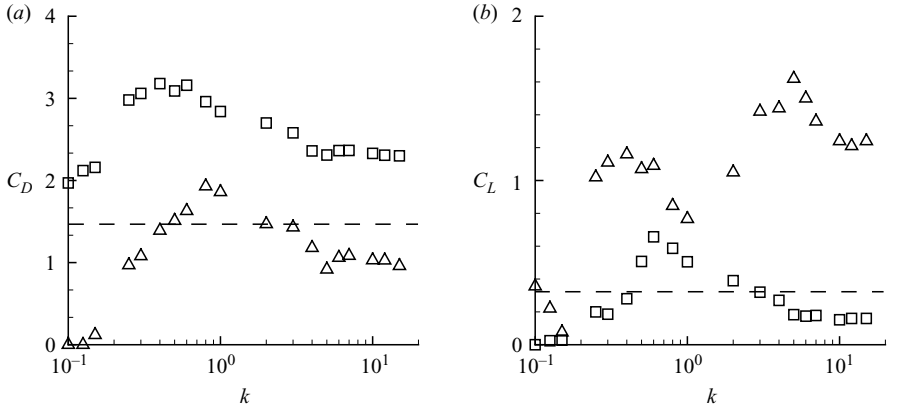


FIGURE 12. (*a*) Mean (□) and second harmonic (△) components of the drag coefficient C_D vs. k. (*b*) First (△) and third harmonic (□) components of the lift coefficient C_L vs. k. The dashed lines indicate the mean drag coefficient (in *a*) and the first harmonic lift coefficient (in *b*) of a fixed rigid cylinder with the same diameter as the undeformed ring.

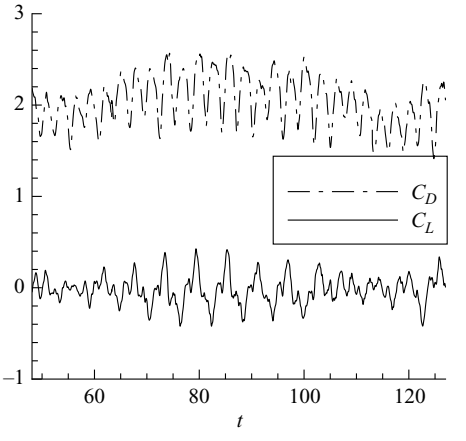


FIGURE 13. Time histories of C_D and C_L at $k = 0.175$.

in the swept area due to body motion (see figures 8 and 9). Except for a small range of k near the resonance, the first-harmonic lift force on the ring is also larger than that on a fixed rigid cylinder. On the other hand, with sufficiently small stiffness (e.g. $k < 0.15$) a flexible ring is seen to sustain smaller mean drag and first-harmonic lift forces than a pinned rigid cylinder (as approached by large values of k).

3.4. *Fluid–structure resonance*

In figures 10 and 12, abrupt changes in the mechanics of the ring are observed across a relatively narrow range of k, $0.15 < k < 0.25$, suggesting the existence of resonance between the flow field and the ring. We herein conduct a close-up study of the system within that range. As an example, time histories of C_L and C_D at $k = 0.175$ are shown in figure 13. C_L displays a beating behaviour, indicating that it includes two dominant frequencies close to each other.

As demonstrated in figure 14, the Fourier analysis of C_L shows that near the first harmonic there exist two frequencies locating at $f_1 = 0.161$ and $f_2 = 0.177$. We note that because of the relatively short simulation time, the accuracy of the Fourier

https://doi.org/10.1017/S0022112009993697 Published online by Cambridge University Press

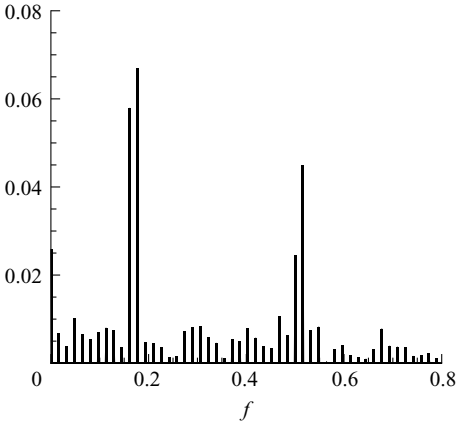


FIGURE 14. Fourier components of the lift coefficient C_L at $k = 0.175$.

analysis is not guaranteed. To ensure the accuracy of these predictions we also employ an alternative approach by fitting the C_L curve shown in figure 13 using a function containing three harmonic components with unknown frequencies, amplitudes and phases via the least-square algorithm. The amplitudes and frequencies of the two leading harmonic components are consistent with results of the Fourier analysis.

A similar behaviour has been reported in studies of reduced models of self-induced and self-sustained oscillations. One of these models, which has been widely used as a mathematical representative of vortex-induced vibration, is based upon the Rayleigh equation or the van der Pol equation of the form

$$\ddot{u} + \omega^2 u = \epsilon \left(\dot{u} - \frac{1}{3}\dot{u}^3 \right) + E(t), \tag{3.3}$$

where u represents the displacement. The excitation $E(t)$ is periodic and has the form $E(t) = \epsilon\kappa cos\, \Omega t$, $(\Omega = \omega + \epsilon\sigma)$. As indicated by Nayfeh & Mook (1979), this system displays complicated responses as $\Omega \sim \omega$. Indeed, close to ω, there exists a 'pull-out' frequency ω_p $(\omega_p > \omega)$. When Ω approaches ω_p from above, the system exhibits a strong beating due to the coexistence of the natural frequency ω and the excitation frequency Ω. When Ω is lower than ω_p, on the other hand, the response contains one dominant frequency with a slow modulation. Such phenomenon has also been discovered in vortex-induced vibrations of a rigid cylinder with two degrees of freedom based upon both numerical and experimental studies (Zhou, So & Lam 1999; Jauvtis & Williamson 2004).

Assuming that the ring behaves similar to a van der Pol oscillator, we conclude that at $k = 0.175$ the natural frequency of the system is 0.161 and the vortex shedding frequency is 0.177.

3.5. *Flow field*

In figure 15, we plot wakes behind the ring with three different stiffnesses, a highly flexible ring ($k = 0.1$), a nearly rigid ring ($k = 1.0$) and a ring undergoing fluid–structure resonance ($k = 0.175$). Interestingly, at these different values of k no qualitative change in the wake signature is observed. Quantitative differences, e.g. the longitudinal distances between neighbouring vortices, do exist owing to slight variations in the vortex shedding frequency (see figure 7). Specifically, the vortex shedding remains in a 2S pattern. It is thus clear that at the Reynolds number we herein consider ($R_e = 100$),

https://doi.org/10.1017/S0022112009993697 Published online by Cambridge University Press

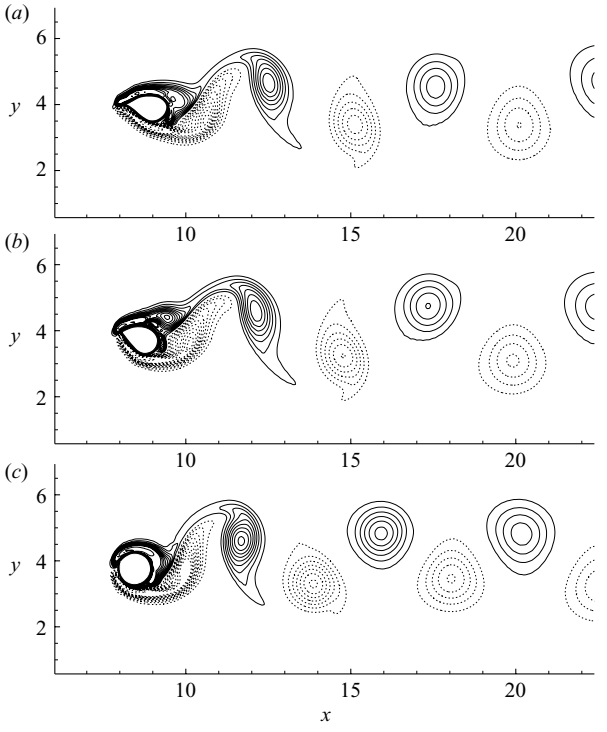


FIGURE 15. The wakes (illustrated by contours of vorticity) behind a ring with (*a*) $k = 0.1$, (*b*) $k = 0.175$ and (*c*) $k = 1.0$. Negative vorticity is shown by dashed lines.

the occurrence of multivortex shedding reported in much higher Reynolds numbers (Jung *et al.* 2006; Dahl *et al.* 2007) does not exist. To illustrate the complicated vortex shedding phenomena and their correlations with ring stiffness, future investigations concentrating on cases with high Reynolds numbers are required.

4. Conclusions

Using an immersed-boundary method, we have numerically investigated the flow-induced vibrations of a deformable ring with one point pinned in space. The ring is modelled as a massless elastic fibre. The numerical algorithm includes a formally second-order Navier–Stokes solver together with a highly efficient spectral method. Its validity and accuracy have been tested and confirmed through comparisons with other numerical models, experiments and asymptotic results.

During flow-induced vibrations, the motion and deformation of the ring consist of several parts, including: (i) a mean deformation, (ii) a rigid-body pitching motion around the pinning point, (iii) a bending deformation in the transverse direction, and (iv) a tapping deformation in the longitudinal direction. Among them the dominant frequencies of the rotation and the bending deformation are the same as the frequency of vortex shedding, while the dominant frequency of the tapping deformation is twice this value. For low-stiffness rings, the tapping deformation becomes negligible. The ring oscillation is dominated by the lateral bending, resembling the deformation of a flag observed experimentally (Taneda 1968; Zhang *et al.* 2000) and numerically (Zhu & Peskin 2002; Connell & Yue 2007). When stiffness is high, the motion is

https://doi.org/10.1017/S0022112009993697 Published online by Cambridge University Press

dominated by the rigid-body rotation. In comparison to a fixed rigid cylinder of the same size, on a pinned flexible ring the hydrodynamic loads (represented by the mean drag force and the first harmonic lift force) are significantly increased as a result of the increased swept area. However, compared with a pinned rigid cylinder the structural flexibility of an elastic ring effectively reduces the hydrodynamic forces.

Fluid–structure resonance is observed when $0.15 < k < 0.25$. Across this range jumps in the ring motion and hydrodynamic loads are discovered. In addition, within this region our numerical simulations show distinctive beating phenomenon in the lifting force. This indicates that despite the complexity of this problem as a result of structural flexibility, it still follows similar fluid–structure interaction mechanisms of reduced models (e.g. van der Pol oscillators) or low-degree-of-freedom systems.

This study was partially supported by the National Science Foundation under grant CBET-0844857. Computational supports from TeraGrid resources provided by the San Diego Supercomputer centre and the National centre for Supercomputing Applications are acknowledged.

Appendix. Asymptotic solutions of the free oscillations of a ring

In § 2.3.2, we employ a perturbation method developed by Cortez *et al.* (2004) to determine the frequencies and decaying rates of free vibration modes of a ring. The key procedure of this method is elaborated below.

In two-dimensional problems, the flow field can be conveniently described through a vorticity field $\omega(\boldsymbol{x}, t)$ and a flow function $\psi(\boldsymbol{x}, t)$. In terms of ω and ψ, and with the immersed-boundary included, the Navier–Stokes equations are expressed as

$$\frac{\partial \omega}{\partial t} + \boldsymbol{u} \cdot \nabla \omega = \nu \nabla^2 \omega + \frac{1}{\rho} \hat{z} \cdot (\nabla \times \boldsymbol{f}) \tag{A 1}$$

and

$$\nabla^2 \psi = -\omega, \tag{A 2}$$

where $\hat{z} \cdot (\nabla \times \boldsymbol{f})$ is the z component (i.e. out-of-the-plane component) of the curl of $\boldsymbol{f}$, the force exerted by the immersed boundary as determined by (2.3). Note that $\boldsymbol{u} = (\partial \psi / \partial y, -\partial \psi / \partial x)$; $\nu = \mu / \rho$ is the kinematic viscosity.

Considering small deformations, the configuration of the ring can be expressed as a summation of static circular shape and a perturbation series as

$$\boldsymbol{X}(s, t) = \boldsymbol{X}^{(0)}(s) + \varepsilon \boldsymbol{X}^{(1)}(s, t) + \cdots, \tag{A 3}$$

where $\boldsymbol{X}^{(0)}$ represents the static state and ε is a small factor characterizing the amount of deformation. Following Cortez *et al.* (2004), the force $\boldsymbol{f}$, the vorticity ω and the flow function ψ are expressed as perturbation series in terms of ε. At $O(\varepsilon^0)$, we have zero vorticity and flow function. Collecting terms in $O(\varepsilon^1)$, we have

$$\frac{\partial \omega^{(1)}}{\partial t} = \nu \nabla^2 \omega^{(1)} + \frac{1}{\rho} \hat{z} \cdot \nabla \times \boldsymbol{f}^{(1)} \tag{A 4}$$

and

$$\nabla^2 \psi^{(1)} = -\omega^{(1)}. \tag{A 5}$$

https://doi.org/10.1017/S0022112009993697 Published online by Cambridge University Press

Expressing $\boldsymbol{X}^{(1)}$ components in r and θ directions as $X_r^{(1)}$ and $X_\theta^{(1)}$, respectively, $\hat{z}\cdot\nabla\times\boldsymbol{f}^{(1)}$ can be written as

$$\hat{z}\cdot\nabla\times\boldsymbol{f}^{(1)} = k\left(\frac{\partial^2 X_\theta^{(1)}}{\partial s^2}+\frac{\partial X_r^{(1)}}{\partial s}\right)\frac{\partial}{\partial r}\left[\frac{\delta(r-R)}{r}\right]-k\left(\frac{\partial^3 X_r^{(1)}}{\partial s^3}-\frac{\partial^2 X_\theta^{(1)}}{\partial s^2}\right)\frac{\delta(r-R)}{r}. \tag{A 6}$$

Also, the ring deformation rate and the flow function are related by

$$\frac{\partial X_r^{(1)}}{\partial t} = \frac{1}{r}\frac{\partial\psi^{(1)}}{\partial\theta}\bigg|_{r=R}, \tag{A 7}$$

$$\frac{\partial X_\theta^{(1)}}{\partial t} = -\frac{\partial\psi^{(1)}}{\partial r}\bigg|_{r=R}. \tag{A 8}$$

Expressing the first-order perturbation of variables in modal form in t and θ, e.g. $\omega^{(1)}=\mathrm{e}^{\mathrm{i}q\theta}\mathrm{e}^{\gamma t}\tilde{\omega}(r)$, the governing equations in $O(\varepsilon^1)$ can be rewritten as

$$\left(\gamma+\frac{\nu q^2}{r^2}\right)\tilde{\omega} = \frac{k}{\rho}(-q^2\tilde{X}_\theta+\mathrm{i}q\tilde{X}_r)\left(\frac{\delta(r-R)}{r}\right)' + \frac{\nu}{r}(r\tilde{\omega}')'+\frac{k}{\rho}(\mathrm{i}q^3\tilde{X}_r-q^2\tilde{X}_\theta)\frac{\delta(r-R)}{r}, \tag{A 9}$$

$$-\frac{1}{r}(r\tilde{\psi}')'+\frac{q^2}{r^2}\tilde{\psi}=\tilde{\omega}, \tag{A 10}$$

$$\gamma\tilde{X}_r = \mathrm{i}q\tilde{\psi}(R), \tag{A 11}$$

$$\gamma\tilde{X}_\theta = -\tilde{\psi}'(R), \tag{A 12}$$

where the primes denote derivatives with respect to r.

We note that the problem can be formulated alternatively by considering the flow fields inside and outside the ring separately, with jumps in $\tilde{\omega}$ and $\tilde{\omega}'$ on the ring as

$$\tilde{\omega}(R^+)-\tilde{\omega}(R^-) = \frac{k}{\nu}(q^2\tilde{X}_\theta-\mathrm{i}q\tilde{X}_r), \tag{A 13}$$

$$\tilde{\omega}'(R^+)-\tilde{\omega}'(R^-) = -\mathrm{i}\frac{k}{\nu}q(q^2-1)\tilde{X}_r. \tag{A 14}$$

Solving the governing equation (A 9) inside and outside the ring, $\tilde{\omega}$ is obtained as

$$\tilde{\omega}(r) = \begin{cases} bJ_q(\mathrm{i}\Omega r), & \text{inside the ring,}\\ aH_q(\mathrm{i}\Omega r), & \text{outside of the ring,}\end{cases} \tag{A 15}$$

where $\Omega=\sqrt{\gamma/\nu}$. Note that J_q and H_q are the qth order Bessel and Hankel functions, respectively; a and b are unknown coefficients. Similarly, by solving (A 10) for the flow function equation $\tilde{\psi}$, we have

$$\tilde{\psi}(r) = \begin{cases} \dfrac{br}{2\mathrm{i}q\Omega}\left[J_{q-1}(\mathrm{i}\Omega r)+J_{q+1}(\mathrm{i}\Omega r)\right]+\dfrac{r^q}{2\mathrm{i}q\Omega}\left[aH_{q-1}(\mathrm{i}\Omega R)-bJ_{q-1}(\mathrm{i}\Omega R)\right], & 0\leqslant r<R,\\ \dfrac{ar}{2\mathrm{i}q\Omega}\left[H_{q-1}(\mathrm{i}\Omega r)+H_{q+1}(\mathrm{i}\Omega r)\right]-\dfrac{r^{-q}}{2\mathrm{i}q\Omega}\left[aH_{q+1}(\mathrm{i}\Omega R)-bJ_{q+1}(\mathrm{i}\Omega R)\right], & r>R.\end{cases} \tag{A 16}$$

https://doi.org/10.1017/S0022112009993697 Published online by Cambridge University Press

Subsequently, $\tilde{X}_r$ and $\tilde{X}_\theta$ can be expressed as a function of a and b; (A 7) and (A 8). Solving for a and b and using the conditions (A 13) and (A 14) lead us to the following eigenvalue problem for the unknown γ ($\gamma = \alpha + \mathrm{i}\beta$, where α and β are the decaying rate and the frequency of mode q, respectively.)

$$[\boldsymbol{M}] \begin{bmatrix} \tilde{X}_r \\ \tilde{X}_\theta \end{bmatrix} = 0, \tag{A 17}$$

where

$$[\boldsymbol{M}] \equiv \begin{bmatrix} M_{11} & M_{12} \\ M_{21} & M_{22} \end{bmatrix}, \tag{A 18}$$

with

$$M_{11} = \mathrm{i}\left\{ \frac{\nu^2\rho}{k}\Omega^3 \left[\frac{H_q(\mathrm{i}\Omega R)}{H_{q-1}(\mathrm{i}\Omega R)} - \frac{J_q(\mathrm{i}\Omega R)}{J_{q+1}(\mathrm{i}\Omega R)} \right] + \mathrm{i}q \right\}, \tag{A 19}$$

$$M_{12} = \frac{\nu^2\rho}{k}\Omega^3 \left[\frac{H_q(\mathrm{i}\Omega R)}{H_{q-1}(\mathrm{i}\Omega R)} + \frac{J_q(\mathrm{i}\Omega R)}{J_{q+1}(\mathrm{i}\Omega R)} \right] - \mathrm{i}q^2, \tag{A 20}$$

$$M_{21} = \mathrm{i}\left\{ \frac{\nu^2\rho}{k}\Omega^4 \left[2 - \frac{H_{q+1}(\mathrm{i}\Omega R)}{H_{q-1}(\mathrm{i}\Omega R)} - \frac{J_{q-1}(\mathrm{i}\Omega R)}{J_{q+1}(\mathrm{i}\Omega R)} \right] + 2q\left(q^2 - 1\right) \right\}, \tag{A 21}$$

$$M_{22} = -\frac{\nu^2\rho}{k}\Omega^4 \left[\frac{H_{q+1}(\mathrm{i}\Omega R)}{H_{q-1}(\mathrm{i}\Omega R)} - \frac{J_{q-1}(\mathrm{i}\Omega R)}{J_{q+1}(\mathrm{i}\Omega R)} \right]. \tag{A 22}$$

The values of α and β are determined by solving $\det[\boldsymbol{M}] = 0$.

REFERENCES

Alben, S., Shelley, M. & Zhang, J. 2002 Drag reduction through self-similar bending of a flexible body. *Nature* **420**, 479–481.

Alben, S., Shelley, M. & Zhang, J. 2004 How flexibility induces streamlining in a two-dimensional flow. *Phys. Fluids* **16**, 1694–1713.

Berger, E. & Wille, R. 1972 Periodic flow phenomena. *Annu. Rev. Fluid Mech.* **4**, 313–340.

Connell, B. S. H. & Yue, K. K. P. 2007 Flapping dynamics of a flag in a uniform stream. *J. Fluid Mech.* **581**, 33–67.

Cortez, R., Peskin, C. S., Stockie, J. M. & Varela, D. 2004 Parametric resonance in immersed elastic boundaries. *SIAM J. Appl. Math.* **65**, 494–520.

Dahl, J. M., Hover, F. S., Triantafyllou, M. S, Dong, S. & Karniadakis, G. E. 2007 Resonant vibrations of bluff bodies cause multivortex shedding and high frequency forces. *Phys. Rev. Lett.* **99**, 144503.

Eldredge, J. D. & Pisani, D. 2008 Passive propulsion of a simple articulated system in the wake of an obstacle. *J. Fluid Mech.* **607**, 279–288.

Engelman, M. S. & Jaminia, M. A. 1990 Transient flow past a circular cylinder: a benchmark solution. *Intl J. Numer. Meth. Fluids* **11**, 985–1000.

Gresho, P. M., Chan, S. T., Lee, R. L. & Upson, C. D. 1984 A modified finite element method for solving the time-dependent,incompressible Navier–Stokes equations. Part 2. Applications. *Intl J. Numer. Meth. Fluids* **4**, 619–640.

Hughes, T., Liu, W. & Zimmerman, T. 1981 Lagrangian–Eulerian finite element formulations for incompressible viscous flows. *Comput. Meth. Appl. Mech. Engng* **29**, 329–349.

https://doi.org/10.1017/S0022112009993697 Published online by Cambridge University Press

Jauvtis, N. & Williamson, C. H. K. 2004 The effect of two degrees of freedom on vortex-induced vibration at low mass and damping. *J. Fluid Mech.* **509** (1), 23–62.

Jung, S., Mareck, K., Shelley, M. & Zhang, J. 2006 Dynamics of a deformable body in a fast flowing soap film. *Phys. Rev. Lett.* **97**, 134502.

Karniadakis, G. E. & Triantafyllou, G. S. 1992 Three-dimensional dynamics and transition to turbulence in the wake of bluff objects. *J. Fluid Mech.* **238**, 1–30.

Kim, J., Kim, D. & Choi, H. 2001 An immersed-boundary finite-volume method for simulations of flow in complex geometries. *J. Comput. Phys.* **171**, 132–150.

Lai, M. C. & Peskin, C. S. 2000 An immersed boundary method with formal second order accuracy and reduced numerical viscosity. *J. Comput. Phys.* **180**, 705–719.

Liao, J. C., Beal, D. N., Lauder, G. V. & Triantafyllou, M. S. 2003 Fish exploiting vortices decrease muscle activity. *Science* **302**, 1566–1569.

Linnick, M. & Fasel, H. 2005 A high-order immersed interface method for simulating unsteady incompressible flows on irregular domains. *J. Comput. Phys.* **204**, 157–192.

Liu, C., Zheng, X. & Sung, C. H. 1998 Preconditioned multigrid methods for unsteady incompressible flows. *J. Comput. Phys.* **139**, 35–57.

Mohandas, N. & Evans, E. 1994 Mechanical properties of the red cell membrane in relation to molecular structure and genetic defects. *Annu. Rev. Biophys. Biomol. Struct.* **23**, 787–818.

Nayfeh, A. H. & Mook, D. T. 1979 *Nonlinear Oscillations*. Wiley.

Papaioannou, G. V., Yue, D. K. P., Triantafyllou, M. S. & Karniadakis, G. E. 2008 On the effect of spacing on the vortex-induced vibrations of two tandem cylinders. *J. Fluids Struct.* **24** (6), 833–854.

Peskin, C. S. 1977 Numerical analysis of blood flow in the heart. *J. Comput. Phys.* **25**, 220–252.

Peskin, C. S. 2002 The immersed boundary method. *Acta Numerica* **11**, 1–39.

Peskin, C. S. & Printz, B. F. 1993 Improved volume conservation in the computation of flows with immersed elastic boundaries. *J. Comput. Phys.* **105**, 33–46.

Roshko, A. 1954 On the development of turbulent wakes from vortex streets. *Tech. Rep.* 1191, National Advisory Committee for Aeronautics (NACA).

Saiki, E. M. & Biringen, S. 1996 Numerical simulation of a cylinder in uniform flow: application of a virtual boundary method. *J. Comput. Phys.* **123**, 450–465.

Spalart, P. R. 1988*a* Direct numerical simulation of a turbulent boundary layer up to $Re = 1400$. *J. Fluid Mech.* **187**, 61–98.

Spalart, P. R. 1988*b* Direct numerical study of leading edge contamination in fluid dynamics of three-dimensional turbulent shear flows and transition. *AGARDCP* **438**, 5.1–5.13.

Taira, K. & Colonius, T. 2007 The immersed boundary method: a projection approach. *J. Comput. Phys.* **225**, 2118–2137.

Taneda, S. 1968 Waving motions of flags. *J. Phys. Soc. Japan* **24** (2), 392–401.

Tezduyar, T. 1992 Stabilized finite element formulations for incompressible-flow computations. *Adv. Appl. Mech.* **28**, 1–44.

Tezduyar, T. 2001 Finite element methods for flow problems with moving boundaries and interfaces. *Arch. Comput. Meth. Engng* **8**, 83–130.

Tseng, Y. H. & Ferziger, J. H. 2003 A ghost-cell immersed boundary method for flow in complex geometry. *J. Comput. Phys.* **192**, 593–623.

Vogel, S. 1996 *Life in Moving Fluids: The Physical Biology of Flow*. Princeton University Press.

Williamson, C. H. K. 1988 Defining a universal and continuous Strouhal–Reynolds number relationship for the laminar vortex shedding of a circular cylinder. *Phys. Fluids* **31** (10), 2742–2744.

Williamson, C. H. K. & Govardhan, R. 2004 Vortex-induced vibrations. *Annu. Rev. Fluid Mech.* **36**, 413–455.

Williamson, C. H. K. & Roshko, A. 1988 Vortex formation in the wake of an oscillating cylinder. *J. Fluids Struct.* **2** (4), 355–381.

Zhang, J., Childress, S., Libchaber, A. & Shelley, M. 2000 Flexible filaments in a flowing soap film as a model for one-dimensional flags in a two-dimensional wind. *Nature* **408**, 835–839.

Zhang, L. J. & Eldredge, J. D. 2009 A viscous vortex particle method for deforming bodies with application to biolocomotion. *Intl J. Numer. Methods Fluids* **59**, 1299–1320.

https://doi.org/10.1017/S0022112009993697 Published online by Cambridge University Press

Zhou, C. Y., So, R. M. C. & Lam, K. 1999 Vortex-induced vibrations of an elastic circular cylinder. *J. Fluids Struct.* **13** (2), 165–189.

Zhu, L. 2008 Scaling laws for drag of a compliant body in an incompressible viscous flow. *J. Fluid Mech.* **607**, 387–400.

Zhu, L. & Peskin, C. S. 2002 Simulation of a flapping flexible filament in a flowing soap film by the immersed boundary method. *J. Comput. Phys.* **179**, 452–468.

Zhu, Q. & Shoele, K. 2008 Propulsion performance of a skeleton-strengthened fin. *J. Exp. Biol.* **211** (13), 2087–2100.

https://doi.org/10.1017/S0022112009993697 Published online by Cambridge University Press